Appendix A

Methodological aspects

A.1 k point generation schemes

Here we shall elaborate on the different **k** point generation schemes and how to estimate the accuracy provided by different sets. Then we shall explain the new **k** point sets which were found by the author to extend the scheme of Cunningham (1974) to the case of two-dimensional hexagonal unit cells.

The quality of a given **k** point set is determined by the amount of error caused in the discrete integration Equation 2.35. We can analyse this error (Chadi & Cohen, 1973) by first expanding the periodic function $f(\mathbf{r})$ to be integrated as a Fourier series

$$f(\mathbf{k}) = f_0 + \sum_{m=1}^{\infty} f_m A_m(\mathbf{k}) \quad , \tag{A.1}$$

where f_n, $n = 0, \ldots$ are the expansion coefficients and $A_m(\mathbf{k})$ are

$$A_m(\mathbf{k}) = \sum_{\mathbf{R}_m} e^{\mathrm{i}\mathbf{k}\cdot\mathbf{R}_m} \quad . \tag{A.2}$$

$\mathbf{R}_m$ contains the real space lattice vectors which are related with the symmetry operations T_i of the symmetry group T, and the subsequent "shells" are ordered so that $0 < |\mathbf{R}_m| \leq |\mathbf{R}_{m+1}|$. The $A_m(\mathbf{k})$ are real-valued and satisfy the following relations:

$$\begin{aligned}
\frac{\Omega}{(2\pi)^3} \int_{\mathrm{BZ}} A_m(\mathbf{k})\, d\mathbf{k} = 0 \quad , \; m = 1, 2, \ldots \\
\frac{\Omega}{(2\pi)^3} \int_{\mathrm{BZ}} A_m(\mathbf{k})\, A_n(\mathbf{k})\, d\mathbf{k} = N_m \delta_{mn} \\
A_m(\mathbf{k} + \mathbf{G}) = A_m(\mathbf{k}) \\
A_m(T_i\mathbf{k}) = A_m(\mathbf{k}) \\
A_m(\mathbf{k})\, A_n(\mathbf{k}) = \sum_j a_j(m,n)\, A_j(\mathbf{k}) \quad ,
\end{aligned} \tag{A.3}$$

where Ω is the volume of the real space primitive cell, N_m is the number of lattice vectors in the shell $\mathbf{R}_m$ and $\mathbf{G}$ is any reciprocal lattice vector.

The value we want is the integral over the first Brillouin zone,

$$\bar{f} = \frac{\Omega}{(2\pi)^3} \int_{\mathrm{BZ}} f(\mathbf{k})\, d\mathbf{k} \quad . \tag{A.4}$$

By inspection of the Equations A.1 and A.4 one immediately notices that

$$\bar{f} = f_0 \quad , \tag{A.5}$$

i. e. the "average" value is just the $R_m = 0$ like always in Fourier transforms and series.

The result of the integral over the set of discrete **k** points 2.35 would be exact if the conditions A.3 would be fulfilled also in the case of the finite **k** point set. This is, however, in general not possible and one has to make a convenient choice of the **k** points. It was shown by Chadi and Cohen that in general the error in integration rapidly decreases with increasing R_m and thus it's best to choose a set which gives zero from as many of the first – *i. e.* shortest – R_m shells as possible. This implies the following condition for the **k** points and their weights:

$$\sum_{\mathbf{k}_i} w_{\mathbf{k}_i} A_m(\mathbf{k}_i) = 0 \ , \quad m = 1, \ldots, N \ . \tag{A.6}$$

As this requirement cannot be fulfilled with a finite number of points there remains error in the sum 2.35 whose magnitude can be obtained from the Equation A.1 multiplying with $w_{\mathbf{k}_i}$ and summing over the k-points:

$$\begin{aligned} \sum_{\mathbf{k}_i} i w_{\mathbf{k}_i} f_0 &= \sum_{\mathbf{k}_i} w_{\mathbf{k}_i} f(\mathbf{k}_i) - \sum_m f_m \sum_{\mathbf{k}_i} w_{\mathbf{k}_i} A_m(\mathbf{k}_i) \\ \Leftrightarrow f_0 &= \sum_{\mathbf{k}_i} w_{\mathbf{k}_i} f(\mathbf{k}_i) - \sum_m{}' f_m \sum_{\mathbf{k}_i} w_{\mathbf{k}_i} A_m(\mathbf{k}_i) \ , \end{aligned} \tag{A.7}$$

where the prime denotes that terms for which the Equation A.6 holds are excluded from the sum. For smooth functions the expansion coefficients decrease rapidly in magnitude and thus by choosing the number of k-points large enough the error can be made negligibly small. Then the sum in the Equation 2.35 becomes a good estimate for the continuous integral,

$$\bar{f} \approx \sum_{\mathbf{k}_i} w_{\mathbf{k}_i} f(\mathbf{k}_i) \ . \tag{A.8}$$

Chadi and Cohen then continued to show that their points for the face centred cubic cell give an error

$$\epsilon \simeq \sum_m{}' \frac{S_m}{|\mathbf{R}_m|^3} \ , \tag{A.9}$$

where $S_m = \sum_{\mathbf{k}_i} w_{\mathbf{k}_i} A_m(\mathbf{k}_i)/N_m = \pm 1$. This form has also been used to evaluate the effectiveness of k-point set in the present work:

$$\epsilon \simeq \sum_m \frac{\sum_{\mathbf{k}_i} w_{\mathbf{k}_i} A_m(\mathbf{k}_i)}{N_m |\mathbf{R}_m|^3} \ . \tag{A.10}$$

As the magnitude of the terms included in the sum decreases rapidly due to the denominator one can terminate the series after rather a small number of shells.

The general procedure to assign the weights w_i on the **k** points is first to give an equivalent weight on all the points in the full Brillouin zone. The lattice symmetry operations, including the inversion,[1] are then applied to find the irreducible part of the Brillouin zone and the **k** points related by a symmetry operation. The weight of a **k** point in the irreducible part of the Brillouin zone is then the number of points related to the current point by the symmetry operations divided by the total number of **k** points in the whole Brillouin zone. For clarifying examples please see below.

A.1.1 Monkhorst–Pack construction of k points

The most straight-forward approach to arrange an integration over a function whose general shape is unknown is to arrange an equidistance grid with a constant distance between the points. Monkhorst

[1]The inversion symmetry in **k** points is always present due to the time-inversion symmetry (Tinkham, 1964)

and Pack (1976) introduced a simple algorithm to obtain the **k** point sets: The points in three dimensions are linear combinations of the reciprocal lattice vectors $\mathbf{b}_1$, $\mathbf{b}_2$ and $\mathbf{b}_3$:

$$\mathbf{k} = n_1\mathbf{b}_1 + n_2\mathbf{b}_2 + n_3\mathbf{b}_3 \ . \tag{A.11}$$

The coefficients n_1, n_2 and n_3 are given by

$$n_i = \frac{2p_i - q_i - 1}{2q_i} \ \ , \ p_i = 1, \ \ldots, \ 2q_i \ . \tag{A.12}$$

The integers q_i are the number of divisions in the three directions. Please note that the Γ point (0,0,0) is contained in the **k** point set only if all q_i's are odd because $\mathbf{b}_1$, $\mathbf{b}_2$ and $\mathbf{b}_3$ are linearly independent and thus n_1, n_2 and n_3 must all simultaneously be equal to zero. Examples of these sets will be given below as their illustration is easier in two dimensions.

Fehlner and Vosko (1977) generalised the Monkhorst-Pack point sets by adding a constant vector $\mathbf{k}_0$ to all the **k** points:

$$\mathbf{k} = n_1\mathbf{b}_1 + n_2\mathbf{b}_2 + n_3\mathbf{b}_3 + \mathbf{k}_0 \ . \tag{A.13}$$

It is easy to verify that these points zero exactly the same cells in the Equation A.6 as the original Monkhorst-Pack points, *i.e.* when $\mathbf{k}_0 = \mathbf{0}$. The advantage of this generalisation becomes obvious when discussing the **k** point sets for the hexagonal cells.

A.1.2 Chadi–Cohen construction of k points

Chadi and Cohen (1973) also gave a practical formula for generating **k** point sets. It is based on using the so-called generating **k** points $\mathbf{k}_1$ and $\mathbf{k}_2$ from which the set is generated by

$$\mathbf{k}_i = \mathbf{k}_1 + \mathrm{T}_i\mathbf{k}_2 \ , \tag{A.14}$$

where T_i is the symmetry operation of the lattice symmetry group. One can straight-forwardly show that if $\mathbf{k}_1$ satisfies the Equation A.6 for shells C_{m_1} and $\mathbf{k}_2$ for shells C_{m_2} then the new points $\mathbf{k}_i$ satisfy it for both C_{m_1} and C_{m_2}. Thus Chadi and Cohen suggested to choose $\mathbf{k}_1$ so as to zero as many shells as possible and to take $\mathbf{k}_2$ which zeroes further as many of the first non-zero shells of $\mathbf{k}_1$ as possible. Note that in the point sets of Chadi and Cohen the generating points or Γ point do not occur in the final sets. Cunningham (1974) applied the Chadi-Cohen procedure to obtain **k** point sets for two dimensional lattices; the case of the hexagonal lattice will be discussed in detail below.

A.1.3 Two-dimensional hexagonal k point sets

In the case of hexagonal super cell there has been an ongoing debate about the relative merits of different **k** point sets (Chadi, 1977; Pack & Monkhorst, 1977; MacDonald, 1978). The problem arose because the original Monkhorst-Pack **k** point sets can not be reduced with the lattice symmetry operations to the smallest possible irreducible part of the Brillouin zone, and since the number of points in subsequent Cunningham sets increases rapidly, thus providing little flexibility in the choice of the set to be used. The addition of a constant "shift" vector to the Monkhorst-Pack points – please see above – enabled the reduction of the Brillouin zone with the full lattice symmetry group but Γ and other extreme points are then included, and below we shall discuss the generalisation of the Cunningham point sets which provides a vast number of new sets between those originally introduced by Cunningham.

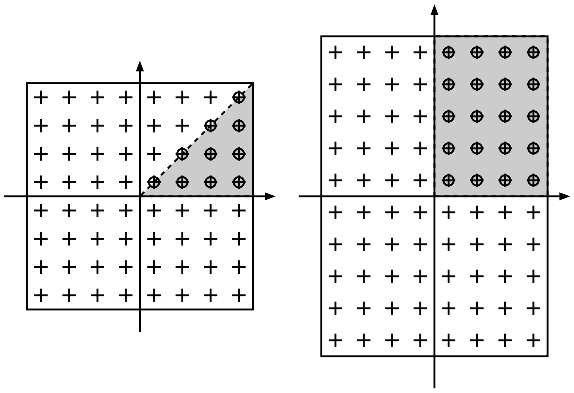

Figure A.1: **k** point sets for two dimensional square and rectangular lattices; the shaded area is the irreducible wedge of the Brillouin zone and the circles the **k** points in it. The division is $q_1 = q_2 = 8$ for the square and $q_1 = 8$, $q_2 = 10$ for the rectangular lattice

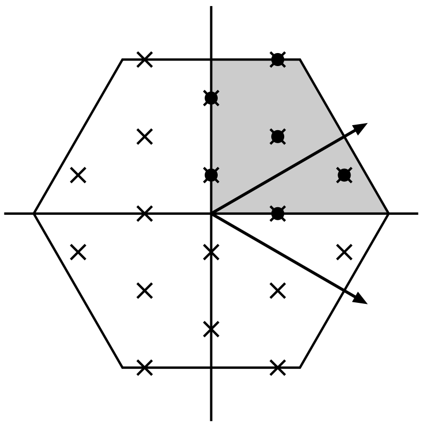

Figure A.2: The **k** point set by the original Monkhorst-Pack scheme obtained with $q_1 = q_2 = 4$; the smmallest wedge of the Brillouin zone which is obtained applying the symmetries of the **k** points is shaded. The arrows show the directions of the reciprocal lattice vectors

Monkhorst-Pack k point sets

We first show the **k** point sets for the square and rectangular cells in the Figure A.1. The square lattice corresponds to a fcc (100) or bcc (100) face and the rectangular to a fcc (110) or bcc (110) face. The division parameters q_1 and q_2 are equal to eight in the square and eight and ten in the rectangular lattice. The regularity of the grid and the avoidance of $\bar{\Gamma} = (0, 0)$ are clearly visible. The latter aspect is why we do not use any constant shift in the set, *i. e.* $\mathbf{k}_0 = \mathbf{0}$, because this way we avoid having any of the corner points in the set.

It is easy to illustrate the problem with the original Monkhorst-Pack points in the hexagonal cells; let us consider the set with $q_1 = q_2 = 4$. Then $n_1 = \pm\frac{1}{8}, \pm\frac{3}{8}$, $n_2 = \pm\frac{1}{8}, \pm\frac{3}{8}$. We show these points in the Figure A.2, and it becomes immediately obvious that the points can have only the symmetry operations identity, inversion, a mirror plane and a two-fold rotation.[2] There the wedge, which can be obtained by reducing using only the symmetries of the **k** set, of the Brillouin zone remains larger than what is possible and more **k** points are needed compared to a set which can be fully reduced in order to obtain the same accuracy.

[2]The two-fold rotation is missing in the real-space lattice symmetry operations of the fcc and hcp lattices due to the stacking

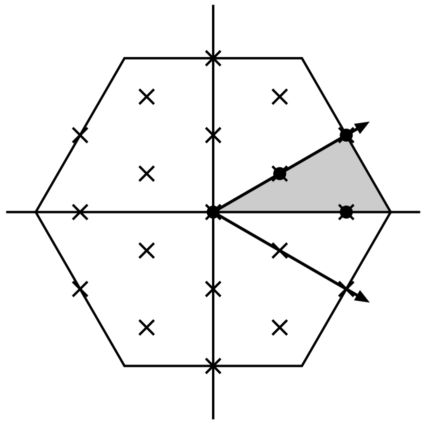

Figure A.3: The **k** point set by the modified Monkhorst-Pack scheme obtained with $q_1 = q_2 = 4$ when k_0 is chosen to have $\bar{\Gamma}$ in the resulting set

Adding a constant **k** vector $\mathbf{k}_0$ which shifts one of the points to the origin $\bar{\Gamma}$ removes this shortcoming and fulfils the whole lattice symmetry group – please see the Figure A.3; thus the irreducible part is only one twelfth of the whole Brillouin zone due to the six lattice symmetry operations[3] plus inversion, altogether twelve separate operations. There appear points also at the outer boundary of the Brillouin zone; this is a general feature of those sets, and has to be taken into account when assigning the weights on the **k** points.

These "shifted Monkhorst-Pack sets" can be easily generated in practise by first drawing an hexagonal equidistance mesh of points centred at $\bar{\Gamma}$. Subsequent sets are then obtained by moving a line – the border of the Brillouin zone – perpendicular to the boundary of the Brillouin zone; whenever the line constitutes a mirror plane an acceptable set is obtained.[4] Note that there are two different ways to form a set depending whether the boundary of the Brillouin zone is perpendicular to $\mathbf{u}_1$ or $\mathbf{u}_2$. Only one of them is given by the shifted Monkhorst-Pack construction; it turns out that they give a better efficiency than the other sets, "30° rotated" sets; the latter will be denoted by a sign $\angle$ below. However, the rotated sets are needed to give equivalent folding of sets in some cells, especially in the hcp $\left(\sqrt{3} \times \sqrt{3}\right)$R30° cell.

Cunningham (two-dimensional Chadi-Cohen) k point sets

Cunningham applied the procedure of Chadi and Cohen to the six two-dimensional Bravais lattices. For the square and rectangular the Cunningham sets form a subset of the Monkhorst-Pack **k** point sets like in the three-dimensional case. On the other hand, the Cunningham sets in the hexagonal lattice are visibly different from the shifted Monkhorst-Pack points – please see the Figure A.4: whereas the shifted Monkhorst-Pack points are arranged on a regular grid the Cunningham points contain "holes", *i. e.* points, which are included in the shifted Monkhorst-Pack sets, are missing. These "holes" are exactly the generating points from the previous smaller set; Cunningham furthermore proposed a two-point set which is not related to the subsequent sets with this "rule", but Chadi later proposed a more efficient two-point set. As it turns out below the **k** point mesh does not have to be uniform in order to zero the shells in the Equation A.6, but these points give even a better efficiency than the shifted Monkhorst-Pack points in sets containing a few points. Moreover,

[3] If the symmetry group is C_{3v} as it is for the fcc(111) and hcp(0001) surfaces. The operations T_i are identity operation, two rotations by $2\pi/3$ and three mirror planes

[4] The mirror plane guarantees the continuation of the translational symmetry of the grid to the next Brillouin zone

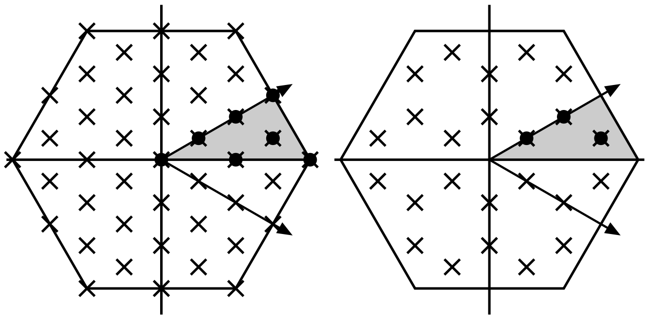

Figure A.4: Examples of the shifted Monkhorst-Pack – *left* – and Cunningham – *right* – **k** point sets

the $\bar{\Gamma}$ and other corner points are avoided in these sets, if this property is regarded as essential.

Extended Cunningham k-point sets

As mentioned above the shortcoming of the Cunningham point sets is that the number of points in subsequent sets increases rapidly whereas the shifted Monkhorst-Pack sets provide sets for almost any number of points. However, by folding the original Cunningham points between different Brillouin zones we found out that there exist many other sets – here called the extended Cunningham point sets – which look exactly like the Cunningham point sets, *i. e.* they contain a "missing point" at the centre of each hexagon; please see the Figure A.4. Like for the shifted Monkhorst-Pack sets we were able to find two groups of different sets, the others being 30° rotated with respect to the others; actually the original Cunningham point sets belong to these two groups alternatingly, for example the six-point set belongs to the "rotated" sets, the 18-point set to the original or un-rotated sets, the 45-point set again to the rotated ones *etc.*

We haven't thought of any "mathematically correct" way how to obtain the extended Cunningham point sets, except naturally choosing the generating points correctly.[5] However, in practise it is trivial to obtain the point sets using the construction scheme given above for the shifted Monkhorst-Pack points: one starts with the equidistance mesh, first removes $\bar{\Gamma}$ from the set as in the Figure A.5, next the point at the centre of the hexagon neighbouring the hexagon around $\bar{\Gamma}$ and continues removing the points at the centres of the neighbouring hexagons. This results into the grid of points in the Figure A.6; the acceptable sets are again obtained by moving a line perpendicular to the vector $\mathbf{u}_1$ or $\mathbf{u}_2$, at the position where the line acts as a mirror plane for the sets inside and outside the first Brillouin zone. Note that the symmetry requirement is now more restrictive than for the shifted Monkhorst-Pack points due to the "holes"; please see the Figure A.8 for examples of rejected sets.

The sets obtained from the scheme above are listed in the Table A.1 and some of them are shown in the Figure A.9. Please note that these sets include all the original Cunningham sets, and also sets with points at the boundary of the Brillouin zone, *e. g.* the set ∠9. The efficiency, defined as the number of shells zeroed in the Equation A.6 divided by the number of points in the set, of the extended sets is also given and it is compared to the efficiency of the shifted Monkhorst-Pack sets in the Figure A.10 and the Table A.1. The few-point sets seem to be better in the extended Cunningham point sets, but for the larger number of points the shifted Monkhorst-Pack point sets give a smaller

[5]Since the extended sets appear exactly like the original Cunningham sets and the subsequent set is obtained by choosing $\mathbf{k}_1$ in the Equation A.14 to be the points in the current set, the extended sets must result from a suitable choice of the initial, one- or few-point set

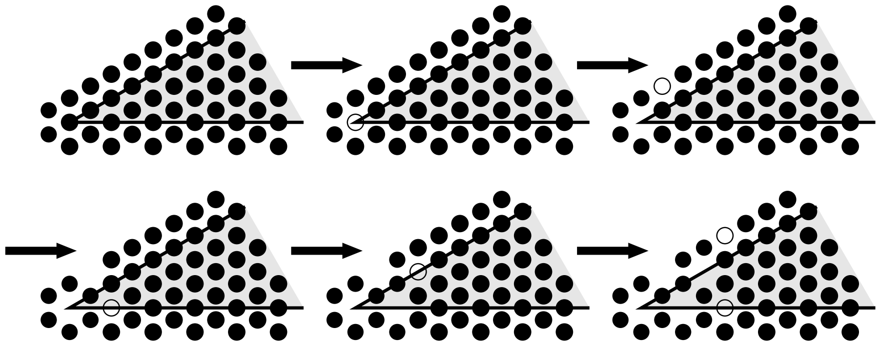

Figure A.5: The procedure to progressively extract the points not belonging to the extended Cunningham sets from the shifted Monkhorst-Pack points

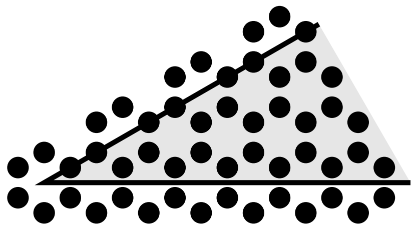

Figure A.6: The grid of the **k** points belonging to the extended Cunningham point sets; the shaded area belongs to the irreducible wedge of the Brillouin zone

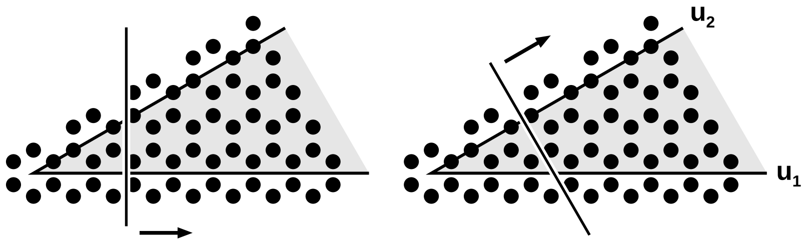

Figure A.7: The procedure to select the extended Cunningham **k** point sets: the line is moved along u_1 or u_2 until some of the valid sets is found. These are obtained when there is a mirror plane perpendicular to $\mathbf{u}_1$ or $\mathbf{u}_2$. The latter leads to the rotated sets $\angle$

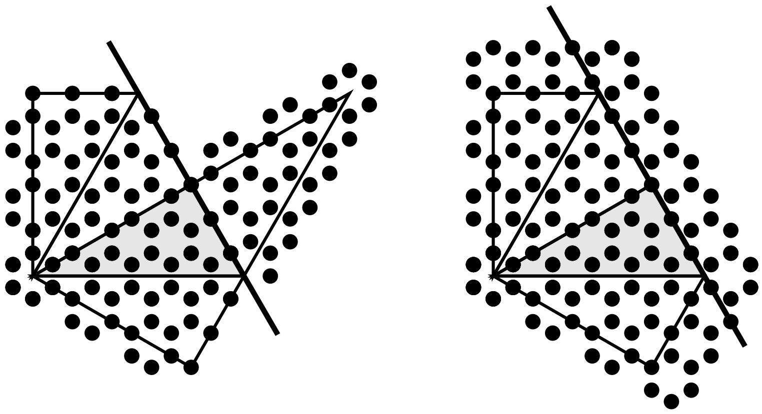

Figure A.8: An example of an invalid set generated with the method of the extended Cunningham sets: the pattern is not continuous – *left* – and there is no mirror plane at the Brillouin zone boundary – *right*

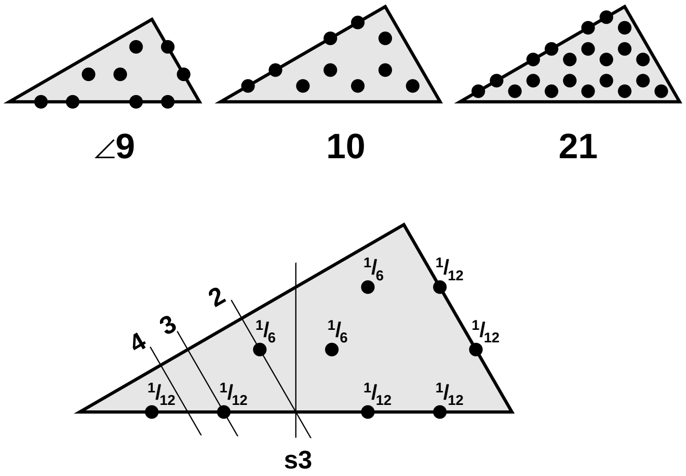

Figure A.9: Examples of the extended Cunningham **k** point sets with $\angle 9$, 10 and 21 points not included in the original work of Cunningham. The lower part shows for the $\angle 9$ point set – used in most of the calculations for ruthenium in the present work – the **k** point weights w_i and folding into $(\sqrt{3} \times \sqrt{3})$R30°, (2×2), (3×3) and (4×4) super-cells. Also folding into at least (2×1), c(2×4) and $(2\sqrt{3} \times 2\sqrt{3})$ is possible

error in the purely mathematical analysis of the error; the physical function to be integrated – the density over the Brillouin zone – often contains the most striking features like surface states at and near the corners of the Brillouin zone. Therefore it remains a matter of importance of these states whether the **k** point set should contain points at these points – shifted Monkhorst-Pack points – or not – extended Cunningham points; in the first case the effects from the $\bar{\Gamma}$ and other corner points might be over-emphasised whereas in the second case a larger number of points is needed before the details at the corners are sampled sufficiently accurately.

A.2 Parallelisation of a plane wave code

Although the computational algorithms and computational power have progressed enormously within the last twenty years the amount of calculations is still huge – all computational capacity can be exceeded at least by growing the system size – and time-consuming; thus although there is no direct way of cutting the amount of computation the through-put time can be reduced by employing parallel processing, *i. e.* splitting the problem to several processors which solve each a part of the task simultaneously. The parallel computer architectures have in recent years developed towards massively parallel processing, with up to thousands of processors; parallelising in such platforms requires large efforts in adapting the traditionally serial programs to efficiently performing parallel codes, and not everyone can afford such large, dedicated machines. Also the parallel execution of a program usually increases the total time of computing compared to several independently running serial programs so parallel processing should be used cautiously and only when it is necessary due to the otherwise too long an execution time or other limitations, *e. g.* disc or memory space.

The plane wave pseudo potential method contains mostly large number of almost independent elements and is thus rather straight-forward to parallelise; there are four different approaches (Clarke, Štich & Payne, 1992) at which level to parallelise the method:

- task-parallel: run the same serial code on several processors; very efficient as long as the

Table A.1: The efficiency of the shifted Monkhorst-Pack and extended Cunningham **k** point sets. Γ, C, E and I show the number of Γ, corner, edge and interior points, respectively, and they have a degeneracy of 1, 3, 6 and 12 when counting the weights of the **k** points if the symmetry group is C_{3v}. $\#k_{BZ}$ is the number of points in the whole two dimensional Brillouin zone, #0 the number of shells zeroed in the Equation A.6 and the last column shows the error estimate of Chadi and Cohen. ∠ indicates that the set is rotated by 30° compared to the unrotated sets; please note that the rotated sets perform worse in the quality

Extended Cunningham

	Γ	C	E	I	$\#k_{BZ}$	#0	CC error
1	0	0	1	0	6	1	4.4290
∠1	0	1	0	0	3	0	—
∠2	0	1	1	0	8	2	2.8687
3	0	0	2	1	24	5	0.5437
∠3	0	0	3	0	18	4	0.8410
∠5	0	1	3	1	32	7	0.3511
6	0	0	3	3	54	11	0.1578
∠7	0	1	4	2	50	10	0.1773
∠9	0	0	6	3	72	14	0.1017
10	0	0	4	6	96	18	0.0654
∠12	0	1	6	5	98	19	0.0631
15	0	0	5	10	150	28	0.0324
∠15	0	1	7	7	128	25	0.0418
∠18	0	0	9	9	162	31	0.0289
21	0	0	6	15	216	39	0.0184
∠22	0	1	9	12	200	37	0.0207

Shifted Monkhorst-Pack

	Γ	C	E	I	$\#k_{BZ}$	#0	CC error
1	1	0	0	0	1	0	—
2	1	1	0	0	4	2	4.8221
∠2	1	1	0	0	3	1	7.4424
3	1	1	1	0	10	4	1.4156
4	1	1	2	0	16	7	0.5916
∠4	1	2	1	0	12	5	0.9154
5	1	0	4	0	25	10	0.2995
∠6	1	1	4	0	27	11	0.2665
7	1	2	3	1	37	14	0.1720
8	1	0	6	1	49	19	0.1070
∠9	1	2	5	1	48	18	0.1106
10	1	1	6	2	64	25	0.0710
12	1	1	7	3	82	31	0.0491
∠12	1	1	8	2	75	28	0.0551
14	1	1	8	4	100	37	0.0353
16	1	0	10	5	121	44	0.0262
∠16	1	2	9	4	108	39	0.0314
19	1	2	9	7	145	51	0.0202
∠20	1	1	12	6	145	52	0.0193
21	1	0	12	8	169	60	0.0154
24	1	1	12	10	196	70	0.0123
∠25	1	2	13	9	192	67	0.0127

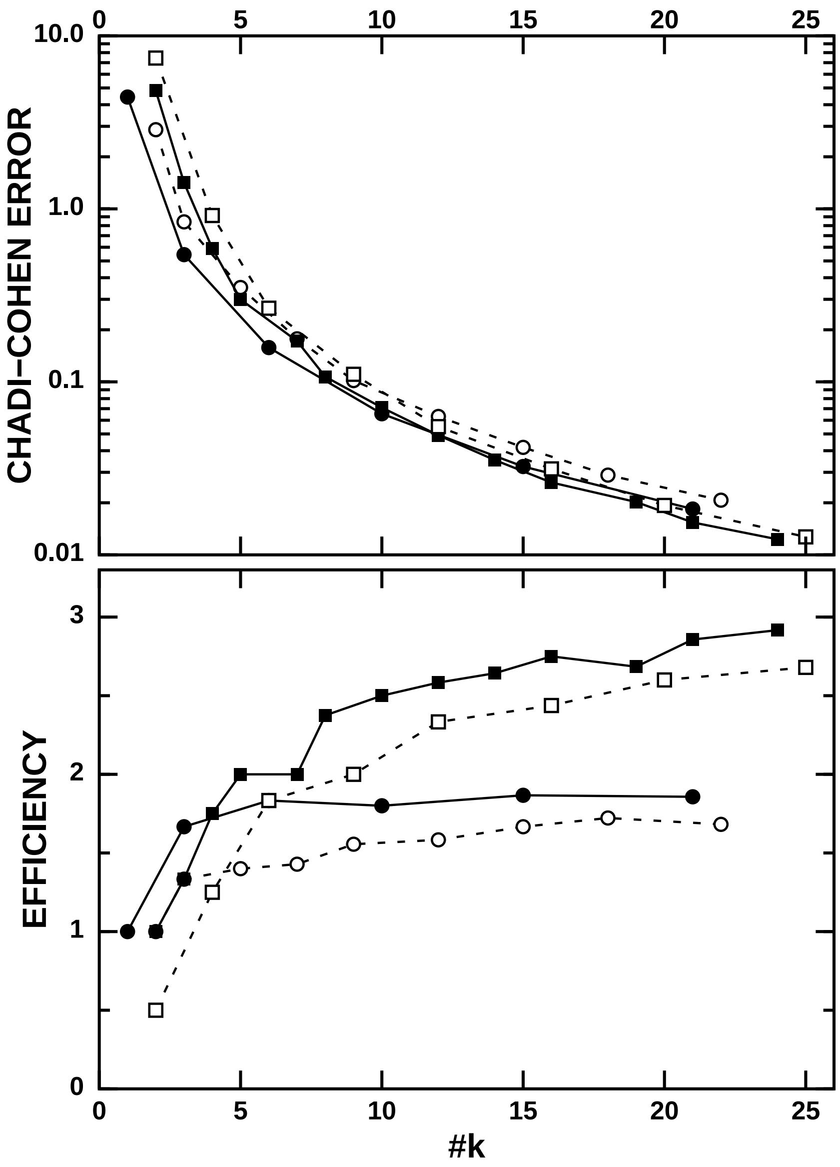

Figure A.10: The error estimate of Chadi and Cohen – upper panel – and the efficiency E – lower panel – for the smallest shifted Monkhorst-Pack – squares – and extended Cunningham – spheres **k** point sets. The dashed lines and empty symbols correspond to the rotated **k** sets. The efficiency is defined as the number of shells zeroed in the Equation A.6 divided by the number of points in the set machines carry enough of memory. This approach is the easiest and cheapest in terms of programming and there is no requirement for inter-processor communication

- **k**-parallel: each node has a part of the **k** points and since the **k** points are almost independent – the density needs to be summed up from all the nodes, furthermore only a couple of trivial operations like determining the occupation numbers; this is the case for the mostly used exchange-correlation functionals, which depend only on the density and not the individual orbitals. The inter-processor communication may be slow, and the amount of additional programming is minimal; however, especially in large systems the number of **k** points is small and this approach can be used only for a couple of processors and hardly ever with more than 8-16 processors. The calculation not explicitly dependent on the **k** points like the density and potential consumes usually only a minor part of the total execution time and thus does not need to be parallelised

- state-parallel: the electronic states are divided to the processors, and they are almost as independent as the **k** points but during the ortho-normalisation of the orbitals – usually with the Gram-Schmidt algorithm – all the orbitals at a **k** point need to be communicated. This causes a lot of simultaneous traffic and thus sets a higher requirement for the network speed and band-width

- plane wave-parallel: as there are lots of plane waves which are independent and operate all the same way the plane wave method is rather easy to parallelise by distributing the calculation at different g vectors to the nodes. However, during the three-dimensional fast Fourier transforms all the g vectors are needed and a very high demand on the communication speed is set; indeed only few massively parallel architectures – like the Cray T3E (`http://www.cray.com/`) – are suited for this approach, but it offers the advantage not available in the aforementioned schemes that also the fast Fourier transform arrays can be split among the nodes; the calculation of the local potential can and must also be easily parallelised since when going to a high number of processors the relative time in its calculation increases. Although this approach is very critical to achieve a good parallel efficiency even over-linear scaling can been achieved because the total amount of the fast cache memory is increased and arrays can now be stored in the memory instead of recalculating thanks to the increased total memory

The different approaches can be combined, *e. g.* the **G**vectors of a **k** are given to a set of processors like shown in the Figure A.11. The best parallel efficiency can be achieved by such groupings, keeping the **G** vector groups as rather small within the limitations from the memory.

The most difficult part in the parallelisation over the plane waves is the three-dimensional fast Fourier transform; however, like mentioned in the Section 2.4.1 it is composed of three subsequent one-dimensional transforms so that the result on one point is not connected to all the other data simultaneously but only the rows with the same $\mathbf{G}_i$ are connected like was discussed in the Section 2.4.1. Therefore a good strategy to minimise the data communication is to divide the **G** vectors to the processors so that all the vectors on one row in one of the directions are on the same processor, and in the real space the grid points are distributed into groups of planes so that after the inverse transform in the third direction the data does not need to be communicated again as shown in the Figure A.12; the forward transform from real to reciprocal space is just the opposite of the backward transform.

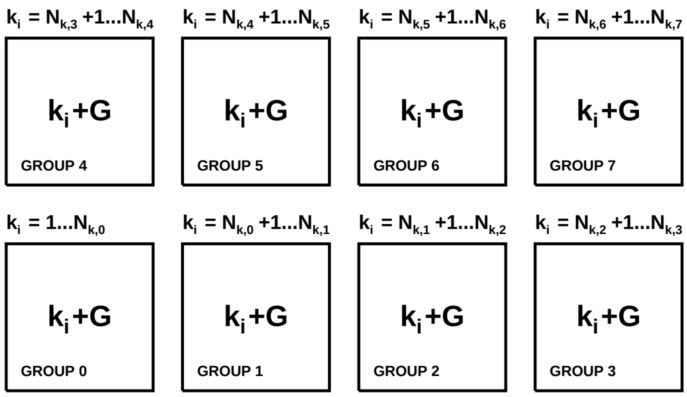

Figure A.11: The grouping of **k** and **G** vectors into two-layer parallelism; in this case the 32 nodes divide the **k** points to the eight groups, and the nodes inside a group further divide the **G** vectors among themselves

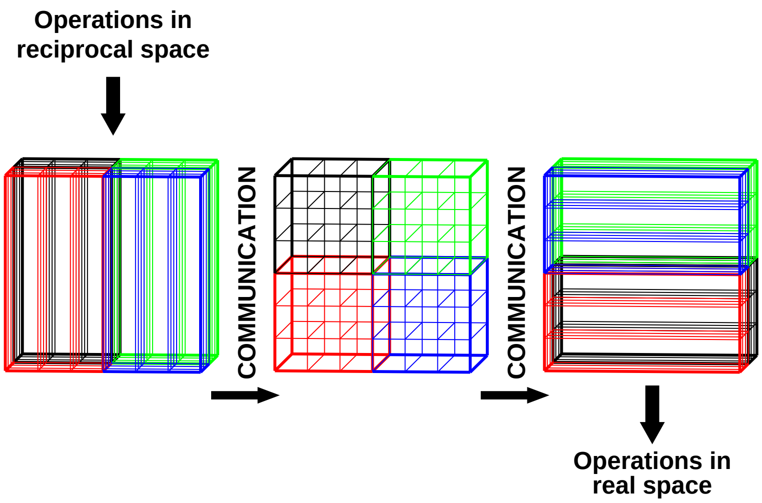

Figure A.12: The distribution of elements in reciprocal and real spaces in order to minimise the communications in the three-dimensional fast Fourier transform; the two operations when changing the direction of the transform correspond to a matrix transpose and a communication both. The columns with different colours belong to the different processors, four in our example

For the wave function a further reduction in the size of data needed to be communicated is achieved by sending only the non-zero data which was described above in the Section 2.4.1.

The parallelisation of the plane wave method is nowadays a standard task and has been documented in the literature; please see *e.g.* Clarke, Štich and Payne (1992), Nelson, Plimpton and Sears (1993) and Brommer *et al* (1993). For example the codes CASTEP/CETEP (Cambridge and Edinburgh/UK), CPMD (Stuttgart/Germany, Zürich/Switzerland), `fhi94md` (Berlin/Germany), FINGER (Helsinki/Finland) and VASP (Vienna/Austria) and the codes used in Lausanne/Switzerland and Trieste/Italy have been parallelised over the G vectors.

A.3 Evaluation of exchange-correlation energy and potential on a discrete grid

The exchange-correlation functional of the homogeneous electron gas is a smooth function and thus the calculations within the local density approximation converge generally easily. However, the functionals of gradient approximations are faster oscillating and therefore more sensitive to the quality of the basis set and numerical algorithms used. Furthermore, since the exchange-correlation term is evaluated on the real space grid it is not invariant of the atomic positions like illustrated in the Figure A.13; even at a cut-off energy of 50 Ry the distance between the grid points is about 0.18 Å and 0.4 Å at 10 Ry cut-off energy. The error does not only affect the energy and potential but also via the self-consistency and, when employing the non-linear core-valence exchange-correlation scheme directly, the forces. While no real solution to this problem has appeared White and Bird (1994) proposed a method which ought to improve the stability and, in some cases, improve the accuracy. Their method will be discussed in a while. Overall the difficulties due to the discrete grid have been studied very little, as the errors from other origins – like the local density approximation, finite basis set, pseudo potentials – have traditionally been much larger than the discretisation error but now, when the calculations are getting more accurate due to the improved computational power, more transferable pseudo potentials *etc* and due to the more frequent use of the gradient approximation, the relative magnitude of this error is emphasised and in our opinion needs special attention.

The problems due to the grid underlying the exchange-correlation energy and potential can arise in various ways:

- The total energy is not constant upon a rigid shift of all atoms in the same direction, without changing the symmetry operations.
- The forces are not zero in a symmetric bulk structure, or they change upon a constant shift of all atoms

It is usually easy to test for the existence and magnitude of the grid effects if their presence is suspected:

- The atoms are set to the original positions, preferably all to the grid points if possible; it has to be recognised here that the symmetries might be broken in the further steps and choose the symmetry operations so that they do not have to be changed later
- All the atoms are shifted by Δz along one axis – here chosen as z – where Δz is the distance of grid points along that axis and the electronic structure is calculated

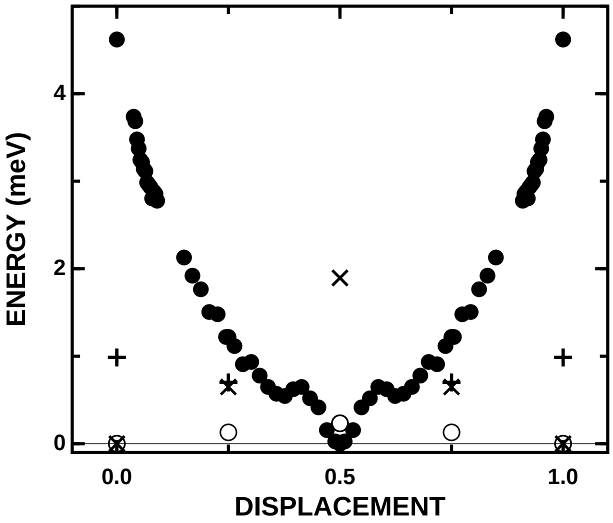

Figure A.13: The error arising from the discrete grid in the evaluation of the exchange-correlation energy and potential: An oxygen atom is moved along one axis between two real-space grid points. The Perdew-Wang'91 functional, a cut-off of 40 Ry for the plane wave basis and duelling 3.2 – filled circles –, 50 Ry/3.85 – crosses –, 70 Ry/4.0 – plus'es – and Perdew-Burke-Ernzerhof functional with 50 Ry/3.85 – empty spheres – were used, the displacement is in units of the grid spacing Δz in the direction of the move and the energy is normalised to its minimum value – at the mid-point between the grid points. Please notice that ideally the line should be zero

- All the atoms are shifted by $\Delta z/2$ in the same direction
- All the atoms are shifted by $\Delta z/4$ in the same direction

If the energy and forces on the atoms are the same in the first two cases but different in the others then the grid affects the results; if furthermore all the atoms were originally on the grid points in the third case there are no artificial forces but the energy different from the first two cases, and in the final case even the forces should be asymmetric.

The functionals with gradients cause a further problem in the un-screening step: at the extrema of the density, where the gradient goes to zero, the functionals become unstable; this leads to rapid oscillations in the unscreened, ionic pseudo potentials like shown in the Figure A.14, and at the origin, or the nucleus, the potential diverges. This is, however, generally not significant because the volume of that point in the integrations is infinitely small and in radial integrals for the Fourier transform of the potentials the integrand is multiplied with r^2 and the origin is not weighted if the divergence is of lower order than squared. Please note that the un-screening Hartree potential is totally smooth and that the newer functional of Perdew, Burke and Ernzerhof (1996) behaves much smoother, and the wiggles at about 0.04 Å from the origin have almost disappeared. Since the discovery of this problem – which now has been recognised to be a consequence of the gradient functionals and not a numerical error (Fuchs, personal communication) – the wiggles were tried to be smoothed out by Ortiz and Ballone (1991) and Juan and Kaxiras (1994), but now it is believed they do not disturb the calculation and thus can be present (Fuchs & Scheffler, submitted).

White and Bird (1994) considered the practical implementation of gradient-augmented functional; they showed how one can implement the potential instead of the straight-forward form

$$\frac{df}{dn} = \frac{\partial f}{\partial n} - \nabla \cdot \frac{\partial f}{\partial (\nabla n)} = \frac{\partial f}{\partial n} - \sum_i \frac{\partial}{\partial x_i} \left[\frac{\partial f}{\partial (\partial n / \partial x_i)} \right] , \tag{A.15}$$

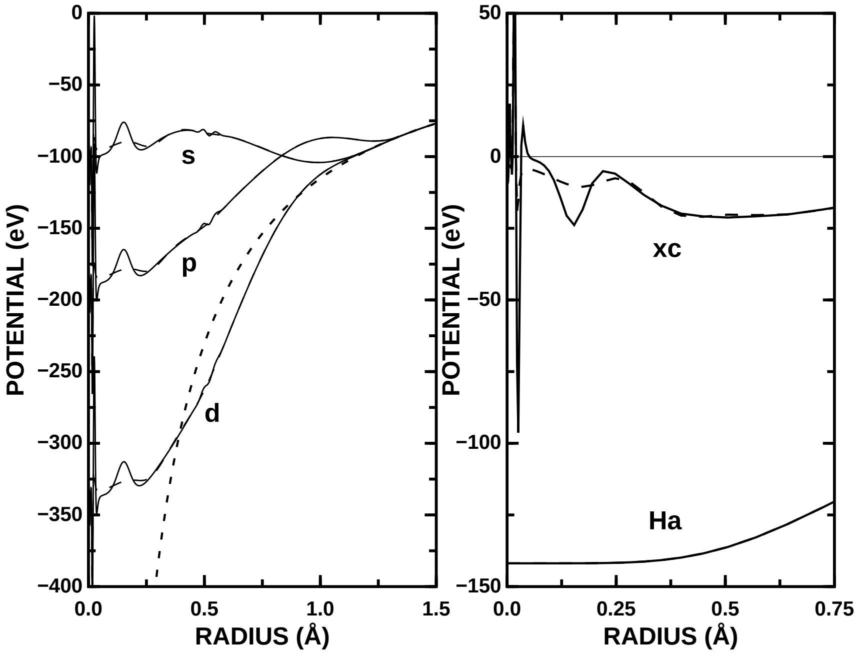

Figure A.14: The wiggles in the pseudo potentials for ruthenium generated with the generalised gradient approximation arising from the un-screening procedure. The left panel shows the ionic pseudo potentials generated using the functional of Perdew-Wang 1991 (Perdew, 1991; Perdew *et al*, 1992; Perdew, Burke & Wang, 1996) – solid lines – and Perdew, Burke and Ernzerhof (1996) – long-dashed lines and the -Z_v/r potential. The right panel shows the un-screening exchange-correlation and Hartree potentials

where f is the exchange-correlation energy per volume, making use of the fast Fourier transforms as

$$\frac{df}{dn} = \frac{\partial f}{\partial n} - \mathtt{FFT}^{-1}\left\{ \mathrm{i}\mathbf{G}\cdot\mathtt{FFT}\left[\frac{\nabla n}{|\nabla n|}\frac{\partial f}{\partial\,|\nabla n|}\right]\right\} \;. \tag{A.16}$$

Thus instead of having to calculate the partial derivatives and to operate to it with the gradient operator $\frac{\partial}{\partial x_i}\left[\frac{\partial f}{\partial(\partial n/\partial x_i)}\right]$ only the partial derivative $\frac{\partial f}{\partial|\nabla n|}$ is needed. The goal of White and Bird was, however, to obtain a numerically efficient and accurate form for the exchange-correlation potential, as they had noticed that if the term

$$\nabla n \cdot \nabla\,|\nabla n| \tag{A.17}$$

is evaluated as written here using the fast Fourier transform the result contains wave lengths shorter than what the discrete grid, set by the cut-off energy, can contain; thus the exchange-correlation energy and potential are not consistent with each other.

However, according to our current understanding (Martin Fuchs, personal communication) this short-coming can be avoided also by using a different form of the term above:

$$\nabla n \cdot \nabla\,|\nabla n| = \nabla n \frac{\nabla n \cdot \nabla\nabla n}{|\nabla|} \;. \tag{A.18}$$

Although the right hand side looks even more complex than the previous form it can be calculated without a need for Fourier transforming any products of already transformed terms, and thus the exchange-correlation energy and potential are consistent. Yet the form which was suggested by White and Bird is easier to implement for a new gradient functional, and it also can be used (Martin Fuchs, personal communication) to evaluate the potential with the knowledge of the energy only by using finite differences of the energy to calculate the gradient in this form:

$$\frac{\partial f}{\partial |\nabla n|} \approx \frac{f(n; |\nabla n| + \delta |\nabla n|) - \partial f(n; |\nabla n|)}{\delta |\nabla n|} \tag{A.19}$$

and similarly for the term $\partial f/\partial n$; here we use for δ a small, positive value. In our tests the resulting potential is insensitive for values $\delta = 10^{-2} \ldots 10^{-7}$.

A.4 Test calculations

We have performed a plenty of test calculations for the transition metals and the atoms and molecules which were adsorbed on the surfaces. All the calculations performed make use of the generalised gradient approximation proposed by Perdew and co-workers (Perdew, 1991; Perdew *et al*, 1992; Perdew, Burke & Wang, 1996), but the newer functional of Perdew Burke and Ernzerhof (1996) yields very similar results.

A.4.1 Ruthenium

The pseudo potential which we used for the ruthenium was of the Troullier-Martins type since the electrons in the 4*d* valence shell are very tightly bound and thus would require an extensive plane wave basis set if the Bachelet-Hamann-Schlüter scheme would be used to construct the pseudo potential. The core radii were taken (Catherine Stampfl, personal communication) as $r_{c,l=sd} = 2.48$ Bohr, $r_{c,l=d} = 2.78$ Bohr and were not refined during the work; this pseudo potential has been seen to work well in our previous calculations *e.g.* for the nitrogen adsorption (Schwegmann *et al*, 1997) on the Ru (0001) or oxygen (Schwegmann *et al*, 1998) on the Ru $(10\bar{1}0)$ surface. The *s* component was used as the local component of the pseudo potential.

Cut-off energy

We first studied the size of the basis set needed to present the ruthenium well; since the convergence is rather insensitive to the environment we used the face-centred cubic bulk lattice as the test system rather than the real lattice of ruthenium, hexagonal close-packed, since in this there are two atoms per unit cell and the number of symmetry operations is lower than in the face-centred cubic lattice. We monitored the lattice constant, bulk modulus, the derivative of the bulk modulus with respect to the pressure and the total energy as a function of the cut-off energy; the results are collected in the Table A.2 and it is evident that already a basis set with a cut-off of 45 Ry would give a good convergence.

k point sampling

Next we checked the **k** point sampling required to approximate the integrals over the Brillouin zone accurately. The calculation of the equilibrium lattice structure in the hexagonal close-packed lattice is time consuming since there are two independent lattice parameters a and c whose values need to be resolved. We performed this by a two-dimensional grid of points over several values, typically $\approx 9 \times 8$, of a and c and fitting then a polynomial of the type

$$E(a, c) = f_0 + f_1 a + f_2 c + f_3 a^2 + f_4 ac + f_5 c^2 + f_6 a^3 + f_7 a^2 c + f_8 ac^2 + f_9 c^3 \tag{A.20}$$

Table A.2: The convergence of the lattice constant a, bulk modulus B and the first derivative B' of the bulk modulus with respect to the pressure of bulk ruthenium in the face-centred cubic cell; the values in the parenthesis are differences in per cent from the value at 80 Ry. Also the total energy relative to the value at 80 Ry is shown

$E_{\mathrm{cut-off}}$ (Ry)	a (Å)	B (MBar)	B'	ΔE (meV)
35	3.879 (−0.21)	2.947 (+1.15)	4.721 (+4.27)	511
40	3.888 (+0.04)	2.838 (−2.60)	4.648 (+2.66)	102
45	3.887 (−0.00)	2.924 (+0.36)	4.500 (−0.62)	16
50	3.887 (−0.00)	2.915 (+0.04)	4.522 (−0.12)	8
60	3.887 (+0.00)	2.916 (+0.06)	4.528 (−0.01)	6
70	3.887 (−0.00)	2.912 (−0.05)	4.535 (+0.15)	3
80	3.887 (≡0)	2.914 (≡0)	4.528 (≡0)	≡0

Table A.3: The optimised lattice parameter a and the c/a ratio, and the total energy of bulk ruthenium in the close-packed hexagonal lattice. Cut-off energy was 60 Ry; although the total energy is not yet fully converged with the largest **k** sets the energies ΔE are given relative to the set 9×4

Set	Sampling	a (Å)	c/a	ΔE (meV)
Cunningham	3×4	2.742	1.623	−417
	6×2	2.774	1.583	−69
	6×4	2.776	1.580	−53
	9×2	2.774	1.585	−14
	9×4	2.780	1.576	—
Monkhorst-Pack	$4 \times 4 \times 8$	2.796	1.548	−89
	$5 \times 5 \times 8$	2.758	1.609	−92
	$6 \times 6 \times 8$	2.786	1.567	+16
	$8 \times 8 \times 8$	2.777	1.581	−25
Experimental		2.70	1.584	

where the f_i, $i = 1, \ldots, 9$ are the fitting parameters. The **k** point sets are referred to as $N_{\mathbf{k}_\parallel} \times N_{\mathbf{k}_c}$ for the Cunningham sets, where $N_{\mathbf{k}_\parallel} \times N_{\mathbf{k}_c}$ is the number of **k** points along the plane in the irreducible wedge of the Brillouin zone which is perpendicular to the c axis and $N_{\mathbf{k}_c}$ is the number of points in the upper space $\mathbf{k}_c > 0$; in the case of the Monkhorst-Pack sets the notation $N_{\mathbf{k}_1} \times N_{\mathbf{k}_3} \times N_{\mathbf{k}_3}$ is used where the $N_{\mathbf{k}_i}$ are the partitions in each direction i in the full Brillouin zone; the point sets were shifted so that perpendicular to the c axis $\mathbf{k}_{xy} = 0$ was included in the set in order to preserve the same symmetry as discussed in the Section A.1.3. The results collected are in the Table A.3 and they show that in the lattice parameters are reasonably well converged when going from the 6×4 to the 9×4 or from the $6 \times 6 \times 8$ to the $8 \times 8 \times 8$ sets. In the main body of the calculations in the present work we used from the set 9×4 the nine points parallel to the two-dimensional Brillouin zone in the slab calculations; the points are shown in the Figure A.9.

Table A.4: Convergence tests for the thickness of the slab of Ru (0001) and the vacuum region with varying number of atomic N_{slab} and vacuum N_{vacuum} layers; given are the total energy per atom, the energy difference E(N)-E(N-1) which eventually would converge to the energy of an atom in bulk, and the work function. The calculations were done on ideal, non-relaxed slab; the relaxation of the outer-most atomic layer did not change the results noticeably

N_{slab}	N_{vacuum}	E(N)/N (eV)	E(N)-E(N-1) (eV)	ϕ (eV)
1	6	−440.812	—	5.807
2	6	−442.229	−443.646	5.179
3	6	−442.602	−443.349	4.995
4	6	−442.755	−443.211	5.177
5	6	−442.869	−443.325	5.157
6	6	−442.938	−443.285	5.143
4	1	−442.784		—
4	2	−442.753		—
4	3	−442.755		5.171
4	4	−442.755		5.172
4	5	−442.755		5.168
4	6	−442.755		5.177

Thickness of slab and vacuum

When the slab geometry is used it is necessary to confirm that the slab is thick enough *i. e.* it has enough substrate layers so that the properties inside the slab approach those of the real bulk, and that the two surfaces do not interact via the slab or the vacuum; the latter is easy to notice if the asymptotic densities from the two surfaces overlap considerably. In the Table A.4 we show the results of a systematic study of the energy and work function as a function of the number of layers in the substrate and the equivalent in vacuum. We can conclude that beyond three to four layers of the substrate the results converge, and already three layers of vacuum, corresponding to about 6,5 Å, is enough to give well converged results. To be on the safe side we employed a five layer slab throughout the calculations of the present work unless otherwise mentioned, and we had about 15 Å of vacuum separating the slab from its own replicas; this distance was mainly dictated by the slow asymptotic decay of the density of the alkali metal cesium.

A.4.2 Oxygen

It turns out that the most stringent requirement for the basis set size is set by the oxygen; thus to have a consistent description of all the systems in the present work we must find a suitable compromise between the accuracy and the size of basis set. We search for this optimum by investigating the properties of the oxygen dimer, namely the bond length, vibrational frequency and binding energy of the oxygen dimer compared to two isolated oxygen atoms. The ground state of the atom and of the oxygen dimer are spin polarised but by the time we were doing these calculations we did not have access to a plane wave code with the spin polarisation implemented, although it is straightforward to program; also the Kohn-Sham scheme, being based on a single determinant for the many bode wave function, gives the ground state of atoms with an open shell as non-spherical (Kutzler

Table A.5: The binding energy of the oxygen dimer as a function of the cubic cell length in our super cell calculation; the values in parenthesis is the deviation in milli electron volts from the result in the largest cell

Unit cell (Bohr)	$E_B(O_2)$ (eV)
10	−6.276 (−84)
11	−6.222 (−30)
12	−6.209 (−17)
13	−6.199 (−7)
14	−6.191 (+1)
15	−6.187 (+4)
16	−6.183 (+9)
17	−6.192 (≡ 0)

& Painter, 1987). The latter is difficult to achieve due to rapid oscillation in the occupation of the states which in principle are degenerate and thus close in the energy. Therefore we obtained the spin energies of the O_2 molecule and the energy difference between a spherical and non-spherical oxygen atom from a calculation employing a cluster program with the same exchange-correlation functional as in our calculations, and the spin energies of the atoms were kindly provided to us by Martin Fuchs (personal communication).

Size of unit cell

First we shall discuss the size of the unit cell necessary to isolate the molecules from each other; the Table A.5 shows the binding energy as a function of the length of the edges of a cubic cell; there remains interaction even beyond a separation of 9 Å, but we estimate the accuracy to be sufficient in a cell of 8-9 Å. Please notice that the unit cell size could probably be somewhat reduced by using a small set of special **k** points instead of the Γ point only like we have done; at the limit of no overlap between the periodically repeated molecules these should be identical but when there remains a small overlap the few **k** points located as to give an average of the weak interaction over the Brillouin zone converge faster than when Γ point only is used since the slightly dispersed bands have extremal values at the Γ point.

Cut-off energy and radii

For the studies aiming at finding a suitable pseudo potential and a sufficient cut-off energy we performed calculations for the oxygen dimer with slightly varying pseudo potential radii and the cut-off energy. The results are collected into the Figure A.15; we see that especially the vibrational frequency does not converge to a reasonably constant value until a cut-off of about 60-80 Ry. Although the value at 40 Ry is closer to the value from experiments and converged calculations it is accidental as is seen from the Figure A.16, which shows the binding energy and the energy adjusted to a common minimum. Clearly the calculations performed at 40 Ry deviate more from the converged results than the results from calculations with an inter-mediate value for the energy cut-off. The error at the low and inter-mediate cut-off energies is at its largest when using the pseudo potentials with the smallest core radii as expected, but the results converge to almost identical

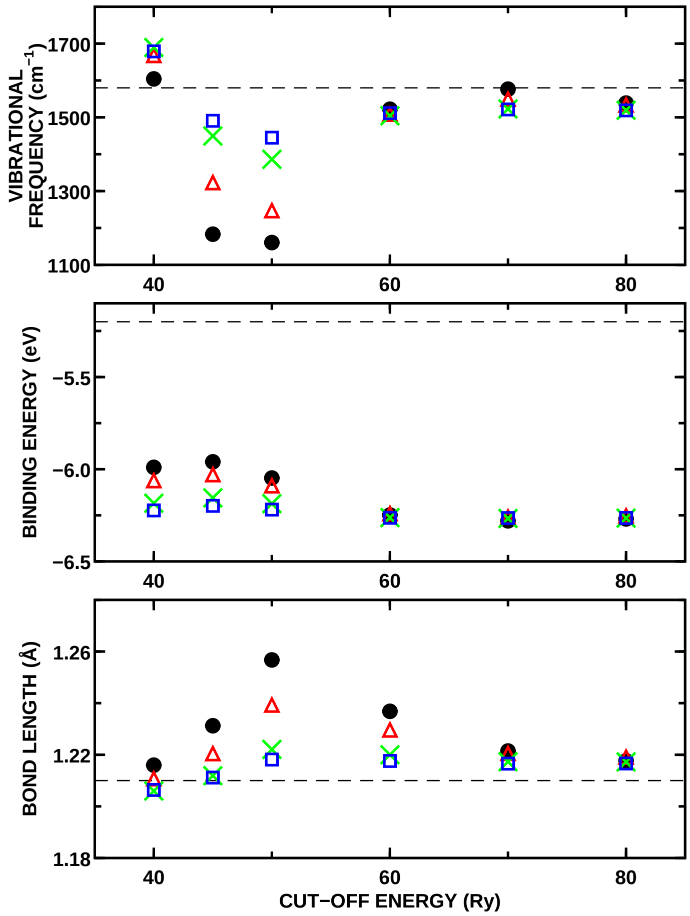

Figure A.15: Convergence test of the molecular properties of an oxygen dimer as a function of the cut-off energy used in the expansion of the Kohn-Sham orbitals in a basis of plane waves. The panels are from bottom to top the bond length in Ångströms, the binding or atomisation energy of the dimer to two isolated atoms and the frequency of the stretching mode vibration of the molecule in inverse centi metres. The horizontal dashed lines are the experimental values. The different markers are for different core radii of the *s* and *p* pseudo potentials – the radius of the *d* potential is irrelevant if it is included – and the markers are for $r_{c,l=sp} = 1.2$ Bohr – filled circles – 1.3 Bohr – triangles – 1.4 Bohr –crosses – and 1.5 Bohr – empty squares

values at the high cut-off energy; thus a large core radius would be justified but it is important that this is only a test for one system. As a compromise between between the accuracy and a reasonable cut-off energy we chose to use 50 Ry with cut-off radii 1.4 Bohr; this settles then the cut-off energy for the system studied in the present work.

A.4.3 Carbon monoxide

To investigate the properties of the carbon monoxide we use basically the same parameters and pseudo potentials as were used for the oxygen as the carbon monoxide are relatively similar molecules.

Cut-off energy

The characteristic properties of the carbon monoxide dimer in the Figure A.17 as the function of the cut-off energy show that these converge slightly earlier, at 40-45 Ry, than the corresponding ones of the oxygen dimer; the core radii of the pseudo potentials of the carbon and oxygen atom are

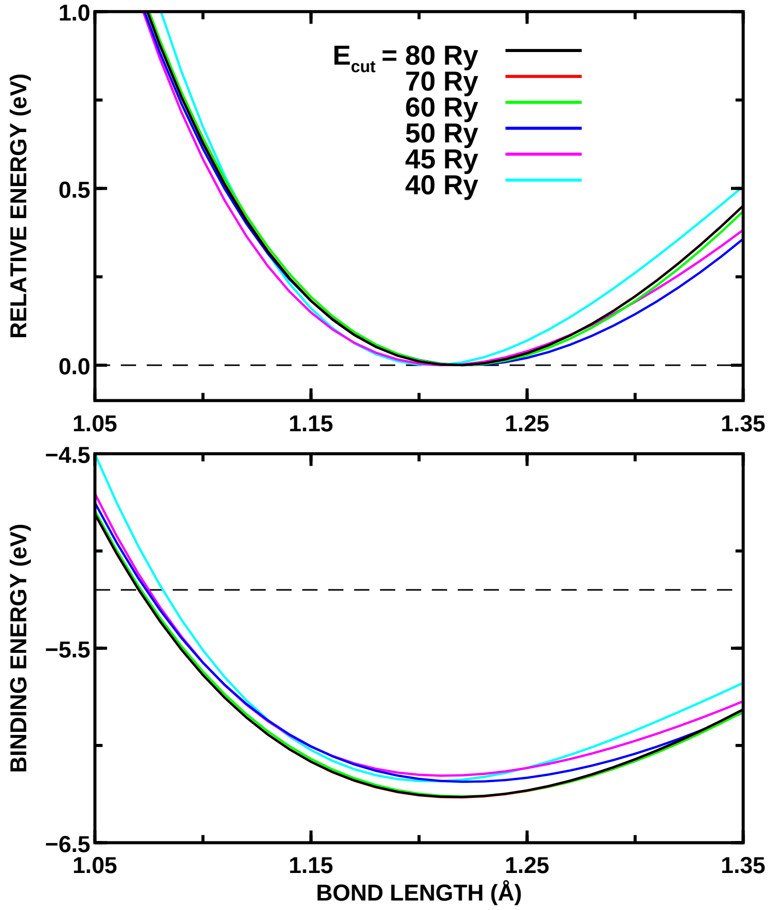

Figure A.16: The energy versus bond length of an oxygen dimer calculated with different values of the cut-off energy; the core radii $r_{c,l=sp} = 1.4$ Bohr. Lower panel: the binding energy of the oxygen dimer, with the experimental value as the horizontal line. Upper panel: the same curves but with normalised to the minimum

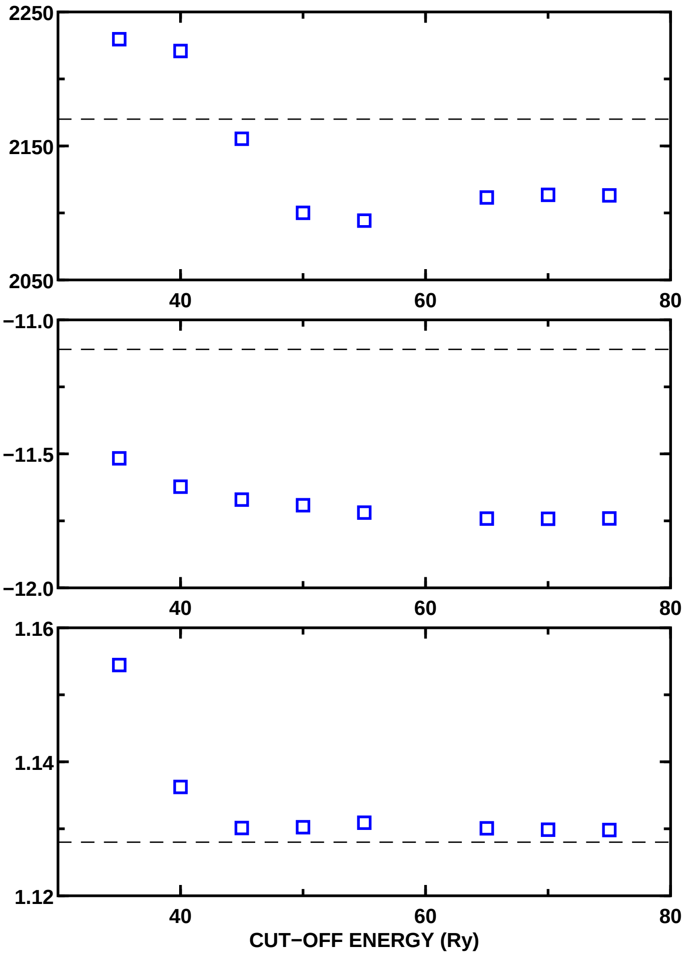

Figure A.17: Convergence test of the molecular properties of an carbon monoxide dimer as a function of the cut-off energy used in the expansion of the Kohn-Sham orbitals in a basis of plane waves. The panels are from bottom to top the bond length in Ångströms, the binding or atomisation energy of the dimer to two isolated atoms and the frequency of the stretching mode vibration of the molecule in inverse centi metres. The horizontal dashed lines denote the experimental values

$r^{\mathrm{C}}_{c,l=sp} = 1.35$ Bohr and $r^{\mathrm{O}}_{c,l=sp} = 1.4$ Bohr. The Figure A.18 further proves that the one-dimensional potential energy surface for stretching the C-O bond length is very well converged already the cut-off energy of 50 Ry.

A.4.4 Cesium

To describe the cesium traditionally a pseudo potential with only the 6*s* in the valence is used; however in this case the pseudo potential must be generated with a largely ionised configuration, thus in the spirit of the Bachelet-Hamann-Schlüter scheme, in order to obtain a transferable pseudo potential. This has probably a justification *a posteriori* not only due to the popular concept of the ionicity of the cesium and especially its 6*s* orbital in different chemical environments but also since the 5*d* and 4*s* are un-bound in the neutral atom but often become also somewhat occupied upon changing to a different surrounding, and these states are lowered and bound when the atom is ionised when part of the charge on the 6*s* is removed.

However since the next orbital, 5*p*, is only 13 eV lower in energy than the eigenvalue of the 6*s* state it can, although fully occupied, at least polarise in different environments and in some

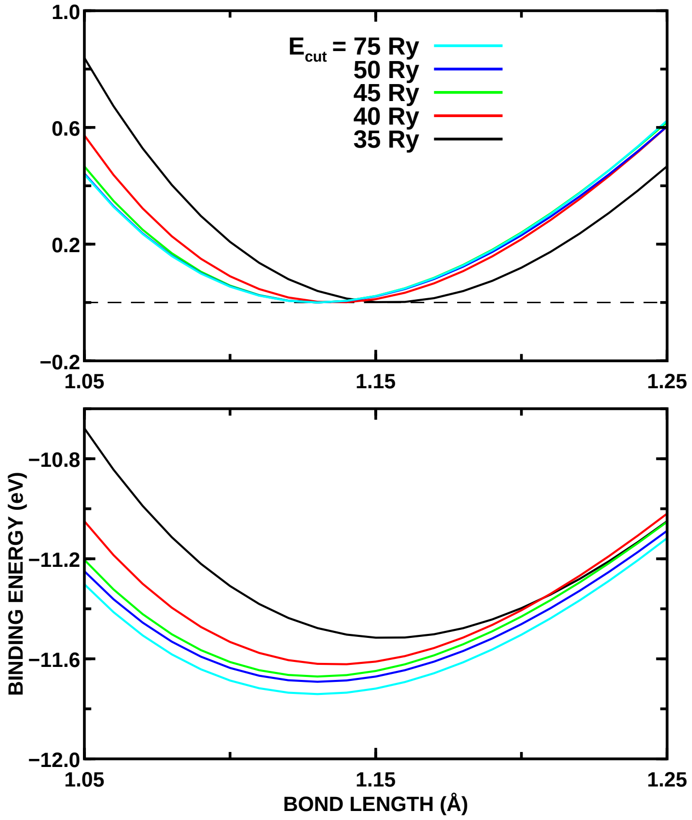

Figure A.18: The energy versus bond length of a carbon monoxide dimer calculated with different values of the cut-off energy. Lower panel: the binding energy of the dimer, with the experimental value as the horizontal line. Upper panel: the same curves but with normalised to the minimum

cases we have seen that this these and even the 5*s* states lie energetically close to the semi-core molecular hybrids of the carbon monoxide. Thus we chose to include the 5*p* as the valence state of the *p* character in the pseudo potential; however then we had difficulties in finding a pseudo potential without ghost states and we were forced to include the 5*s* state as the valence state with the *s* character since we had not implemented a scheme to treat different radial states with the same *l* quantum number in the pseudo potential. Thus the 6*s* is obtained as the first excited state of the pseudo potential constructed for the 5*s* state; please see the Figure A.19 where the electronic pseudo orbitals and the orbital obtained for the 6*s* are shown. In this construction the quality and transferability of the pseudo potential largely relies on how the pseudo potential constructed from the 5*s* state describes the relevant changes in the energy region of the 6*s* eigenvalue. A further alternative to insure the transferability and good description of the 6*s* state would be the use of several projectors at different energies in the pseudo potential like present *e.g.* in the Vanderbilt ultra-soft pseudo potentials. The core radii were chosen (Martin Fuchs, personal communication) as r_c = 2.3, 2.6 and 3.2 Bohr for the 5*s*, 5*p* and 5*d* channel respectively.

Cut-off energy

We tested the required cut-off and the quality of the pseudo potential in the body centred cubic lattice of bulk cesium; we also did some calculations in cesium chloride and face centred cubic lattice of cesium but these calculations shall not be discussed here. The Table A.6 shows the convergence of the relevant lattice properties with an increasing cut-off energy. The lattice constant is almost four per cent larger than in the experiments – and we haven't even included the zero-

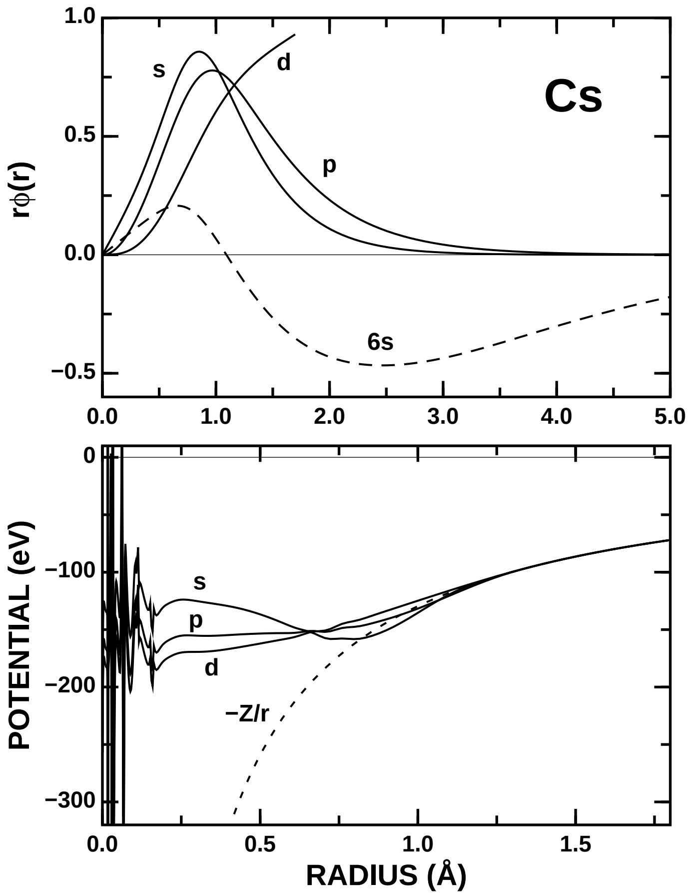

Figure A.19: The pseudo potentials – lower panel – and the pseudo orbitals of the potential used in the present work for cesium; the wave functions have been multiplied with the radius. Please notice that the 5*s* state is node-less but its first excited state, describing the 6*s* state, has a radial node

Table A.6: The convergence of the lattice constant a, bulk modulus B, the first derivative B' of the bulk modulus with respect to the pressure, the total energy, and the cohesive energy of bulk cesium in the body centred cubic cell; the values in the parenthesis are differences in per cent from the value at 80 Ry

$E_{cut-off}$ (Ry)	a (Å)	B (MBar)	B'	ΔE (meV)	E_{coh} (eV)
35	6.283 (−0.04)	0.021 (+18.66)	1.393 (+62.80)	580	0.61
40	6.289 (+0.05)	0.018 (+1.27)	3.845 (+2.69)	275	0.62
45	6.287 (+0.02)	0.018 (+0.83)	3.749 (+0.15)	154	0.61
50	6.286 (+0.00)	0.018 (+0.11)	3.823 (+2.12)	129	—
60	6.286 (+0.01)	0.018 (+0.44)	3.688 (−1.50)	106	0.62
80	6.286 (≡ 0)	0.018 (≡ 0)	3.744 (≡ 0)	≡ 0	—
Expr.	6.05	0.020		—	0.80

point corrections to our results – and thus slightly more than the usual 1...3 %; however all the properties of the lattice converge well already below 50 Ry and are reasonably close to the experiments, giving reliability to our pseudo potential and the numerical method in general. The cohesive energy was extracted using the energy of the cesium atom in a simple cubic super cell with the edge length of 35 Bohr; this was found to be sufficient to converge the energy to within milli electron volts, but such a large cell is required due to tell very large extent of the weakly bound 6*s* orbital. The spin energy of 0.12 eV within the generalised gradient approximation of Perdew *et al* (1991) of the cesium atom was again obtained from Martin Fuchs (personal communication).